Chemical Science

ROYAL SOCIETY OF CHEMISTRY

EDGE ARTICLE

View Article Online
View Journal

Cite this: DOI: 10.1039/d6sc00138f

All publication charges for this article have been paid for by the Royal Society of Chemistry

Received 6th January 2026
Accepted 9th April 2026

DOI: 10.1039/d6sc00138f

rsc.li/chemical-science

Nuclear quantum effects amplify autoionization-driven superionic behaviour in nanoconfined monolayer water

Pavan Ravindra,[ab] Xavier R. Advincula,[acd] Benjamin X. Shi,[ad] Samuel W. Coles,[ad] Angelos Michaelides [*ad] and Venkat Kapil [*adef]

While nuclear quantum effects influence autoionization in ambient-condition bulk water, their impact on autoionization-driven phase transitions is only observed at extreme conditions (in the range of many tens or hundreds of GPa). Here, we show that, for a monolayer of water in uniform nanoconfinement, nuclear quantum effects induce a superionic phase transition under milder conditions than in bulk. Our calculations suggest that this effect brings superionic behaviour into pressure regimes much closer to those accessible in current 2D-material-water encapsulation experiments.

Introduction

Despite its simple molecular structure, water exhibits complex phase behaviours. The known phases of bulk water include over eighteen crystalline ice phases,[1] several amorphous ice phases,[2–5] and possibly two distinct liquid phases in the supercooled regime.[6]

This complexity of water's phase diagram is maintained when it is confined to nanometer-scale cavities.[7–12] The stable phases of nanoconfined water are generally made up of 1–3 layers of water molecules.[8–10] The structures and properties of these phases differ dramatically from the bulk,[13–16] and atomistic simulations have played a pivotal role in their exploration. Traditional empirical force fields have been useful in identifying several of these novel phases.[7,11,17–21] However, because they are not parameterised for the properties of confined water, they do not reliably determine where these phases lie within the confined-water phase diagram.[11,22] Accordingly, studies have instead employed first-principles calculations to explore the stable phases of nanoconfined water.[20,21,23] Machine learning interatomic potentials (MLIPs) have extended these studies by predicting the phase diagrams of water confined within graphene-like cavities ranging from 5 to 8 Å in width.[8–10,24,25]

An intriguing outcome of nanometer-scale confinement, as predicted by simulations,[8,10] is the reduction in the onset conditions for superionic proton transport in water. In superionic phases of water, protons hop between immobile oxygen sites, resulting in high ionic conductivity.[26–29] In bulk water, superionic proton transport emerges only under extreme temperature and pressure conditions, on the order of hundreds of GPa and thousands of kelvin.[27,28] However, Kapil *et al.*[8] predicted that monolayer water in 5 Å graphene-like cavities could exhibit superionic behaviour in the 9–12 GPa range and hundreds of Kelvin. These predictions did not incorporate quantum nuclear effects (NQEs) in the motion of protons. Jiang *et al.*[10] further explored the 6–8 Å range of confinement width and a larger range of pressures and temperature up to 100 GPa and temperatures up to 2000 K. Although NQEs were not probed at a confinement width of 5 Å, the authors emphasised their importance for superionic proton dynamics in 6–8 Å wide cavities at pressures of tens of GPa and temperatures exceeding 600 K.

These studies – together with renewed experimental interest in probing NQEs[30,31] – raise the question of whether NQEs can further reduce the onset conditions of superionic water under nanoconfinement. Although NQEs in bulk water often lead to a near cancellation due to competing quantum effects,[32–34] resulting in NQE-driven phase transitions only at extreme pressures (*e.g.* in the tens of GPa range[35]), recent experiments suggest that translational symmetry breaking at interfaces prevents complete cancellation, allowing net NQEs to be observed.[31] This observation raises the question of whether similar behaviour occurs for nanoconfined water at a confinement width of 5 Å – the regime in which superionicity is known to occur at the lowest temperatures and pressures. Such an effect would be intriguing for laboratory realisation of

[a]Yusuf Hamied Department of Chemistry, University of Cambridge, Lensfield Road, Cambridge, CB2 1EW, UK. E-mail: am452@cam.ac.uk; v.kapil@ucl.ac.uk
[b]Department of Chemistry, Columbia University, 3000 Broadway, New York, NY 10027, USA
[c]Cavendish Laboratory, Department of Physics, University of Cambridge, Cambridge, CB3 0HE, UK
[d]Lennard-Jones Centre, University of Cambridge, Trinity Ln, Cambridge, CB2 1TN, UK
[e]Department of Physics and Astronomy, University College London, 7-19 Gordon St, London WC1H 0AH, UK
[f]Thomas Young Centre and London Centre for Nanotechnology, 9 Gordon St, London WC1H 0AH, UK

superionic water, as current onset conditions are nearly an order of magnitude beyond experimental reach.[7]

In this work, we quantify the impact of NQEs on autoionization in monolayer water confined to a narrow 5 Å-wide channel. We probe the vicinity of the temperature–pressure range that exhibits superionic behaviour under classical nuclear motion.[8] Contrary to expectations based on bulk water, we find that NQEs trigger substantial proton delocalisation in both the ordered (solid) and disordered phases. This results in a surge in proton shuttling in the solid phase and enhanced proton transfer in the disordered phase, resulting in a dramatic reduction of the onset pressure for superionic proton transport to 6 GPa – well below previously reported values for nanoconfined water.[8,10] Our work bolsters the argument that interfaces can exhibit heightened NQEs and bring the onset conditions closer to experimentally accessible regimes.

Methods

Our simulation setup mimics a monolayer film of water trapped between two sheets of graphene.[7] We model the water–carbon interactions using a flat confining potential fit to quantum Monte Carlo (QMC) calculations.[23] Such a setup has been used in previous simulation studies of graphene-like nanocapillaries[8–11,23] and has also been compared to setups containing explicit carbon atoms.[7,21,36] We incorporate water–water interactions at the revPBE0-D3 (with zero damping) level using the Behler-Parrinello MLIP[37] from ref. 8. This functional has previously been validated against QMC calculations of confined ice.[22] We further assess the accuracy of this functional for reactive events in Section II of the SI (SI) by estimating the potential energy barrier for proton transfer in monolayer superionic water at the level of coupled cluster theory with single, double, and perturbative triple excitations (CCSD(T)) with a local approximation.[38] The revPBE0-D3 functional achieves better than chemical accuracy regarding the forward reaction barrier.

Classical and path integral MLIP simulations are performed using i-PI v2.0 (ref. 39) and the LAMMPS-n2p2 interface.[40,41] We employ the recently developed Path Integral coarse-Grained Simulations technique to reduce the high cost of running centroid molecular dynamics.[42] For the path integral simulations, we estimate equilibrium properties, such as free energy profiles, by averaging over all replicas. We estimate dynamical properties, like mean squared displacements and ionic conductivities, by using the dynamics of the centroids.[43] Further computational details are provided in Section I of the SI.

Results

In Fig. 1(a), we report a part of the phase diagram from ref. 8 spanning the 1–12 GPa lateral pressure range. Under these pressures, the stable phase at low temperatures is the solid flat-rhombic phase, depicted in Fig. 1(c). Kosterlitz–Thouless–Halperin–Nelson–Young (KTHNY) theory for two-dimensional phase transitions predicts that two-dimensional solids should melt through a two-step melting process.[44,45] This two-step mechanism can be seen in Fig. 1(a) along the 1 GPa lateral pressure isobar. Along this isobar, the flat-rhombic phase undergoes an initial phase transition to a hexatic phase at around 320 K, followed by a second phase transition to a liquid phase around 460 K. One hallmark of the intermediate hexatic phase is the six-fold orientational order in its oxygen sublattice, which can be seen in Fig. 1(d). This six-fold orientational order is lost in the liquid phase, shown in Fig. 1(e). Fig. 1(a) also shows that the hexatic phase exhibits superionic proton transport at higher temperatures and pressures, indicated by the hatched yellow region. In this superionic hexatic phase, the hexatic oxygen sublattice remains fixed, while protons readily diffuse through the hexatic sublattice.

In Fig. 1(b), we report the changes in phase behaviours when NQEs are included. It is well known that NQEs do not activate the long-ranged and low-energy intermolecular modes that induce a global reordering of molecules in water.[32,46,47] Consistent with this notion, we do not observe changes across the solid-to-liquid phase transitions with the inclusion of NQEs. In contrast, we observe significant changes in the proton phase behaviour with the inclusion of NQEs. Similar behaviours are observed in high-density bulk ice phases due to intramolecular O–H fluctuations.[29,35,48] While these changes in proton phase behaviour occur in bulk at tens or hundreds of GPa, the changes we observe under nanoconfinement occur at much lower lateral pressures, in the 1–12 GPa range.

To determine whether NQEs induce proton transfer in nanoconfined water, we compute the free energy profiles along the proton transfer coordinate ν for the protons in our simulations. ν is defined such that protons with large absolute values of ν are much closer to their nearest oxygen atom than they are to their second nearest oxygen atom. Conversely, protons with ν near 0 are equidistant from their two nearest oxygen atoms. In order for a proton to transfer from one oxygen atom to another, it must pass through $\nu = 0$. Hence, the height of the free energy barrier at $\nu = 0$ provides information about the rate of proton transfer between oxygen atoms. The mathematical definition of the ν coordinate and an illustrative figure are provided in Section III of the SI.[49–51] Although we refer to ν as the proton-transfer coordinate, following conventional usage in the literature, it should not be understood as the full reaction coordinate for proton transfer in water. For instance, the collective reorganisation of nearby water molecules is known to be critical for proton transport in bulk water,[52] but these are not included in the definition of ν.

We first investigate the influence of NQEs on proton transfer in the flat-rhombic phase at 12 GPa. With a classical description of nuclear motion, protons remain bound to their nearest oxygen atoms on the (nanosecond) timescale of our simulations. This remains true up to the hexatic phase transition near 300 K. The red curves in Fig. 2(b) illustrate this, as they never reach $\nu = 0$. Since no proton transfer events are observed within the timescale of our simulations, we are unable to determine the classical free energy barrier. In contrast, our simulations that account for NQEs exhibit low free energy barriers for proton transfer, even at temperatures as low as 100 K. Therefore, we

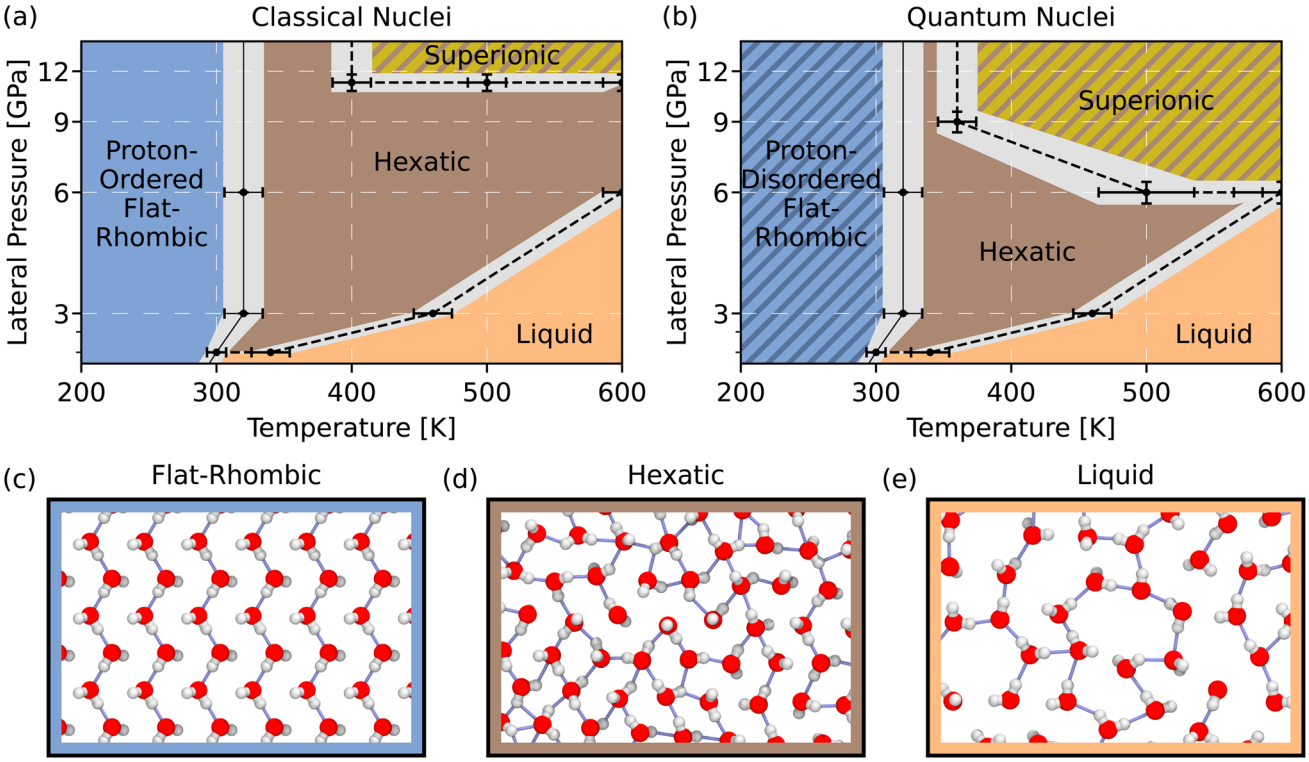

Fig. 1 Impact of nuclear quantum effects on the phase diagram of nanoconfined water. (a) A portion of the phase diagram of nanoconfined water, computed with classical nuclei. The grey regions represent the regions of uncertainty associated with the phase boundaries. (b) The same portion of the phase diagram with nuclear quantum effects taken into account. The detailed procedure for computing these phase diagrams is provided in Section I of the SI. (c)–(e) Snapshots of the (proton-ordered) flat-rhombic phase, hexatic phase, and liquid phase, respectively. These snapshots show a zoomed-in portion os the simulation cell from our simulations with classical nuclei.

conclude that NQEs enable proton delocalization between neighboring water molecules in the flat-rhombic phase.

To further characterize the proton delocalization mechanism, we compute the joint free energy distribution of the proton transfer coordinate ν and the distance between the two oxygen atoms involved in the proton transfer d_{OO}. The two-dimensional profiles in Fig. 2(c) exhibit two significant differences between the classical and quantum cases. First, the range of d_{OO} distances narrows with the inclusion of NQEs, indicating that the oxygen atoms are closer together in the quantum simulations. Second, for the same d_{OO} values, proton delocalisation is significantly enhanced by NQEs compared to classical simulations. Overall, NQEs promote proton delocalisation along the transfer coordinate into regions that are not sampled in our classical simulations.

We next examine the mean-squared displacement of protons to determine whether the reduced barrier along the proton-transfer coordinate facilitates proton transfer. As shown in Fig. 2(d), NQEs do not induce proton transfer, despite the enhanced proton delocalisation. This is intuitively observed by comparing the classical and quantum snapshots in Fig. 2(a). In the classical snapshot, the hydrogen bond network is ordered, with protons covalently bonded to the oxygen above them. In the quantum snapshot, some protons are covalently bonded to the oxygen above, while others are bonded to the oxygen below. In these simulations, protons dynamically shuttle between the same two oxygen atoms, explaining the lack of long-range diffusion. The bulk ice VII phase exhibits similar behaviour at room temperature but at much higher pressures in the 40–50 GPa range.[35] Classical ice VIII is proton-ordered, while NQEs induce a phase transition into ice VII with facile sharing of protons between hydrogen-bonded oxygen atoms. Compared to bulk, NQEs induce proton sharing in nanoconfined flat-rhombic ice at much lower pressures—down to 1 GPa (see Section IV of the SI)—likely due to the short hydrogen bonds in this phase.[24]

The differences caused by NQEs in the hexatic phase at 4 GPa are even more marked. Ref. 8 estimates the ionic conductivity of the hexatic phase using classical linear response theory. At around 400 K, the ionic conductivity is shown to exceed 0.1 S cm^{-1}, which is the threshold for superionic behaviour that we will use in this work as well.[53] Fig. 3(a) shows snapshots that compare our classical and quantum simulations at 400 K. These snapshots do not exhibit any appreciable qualitative difference between classical and quantum superionic hexatic water. However, Fig. 3(b) shows that NQEs lower the barrier along the proton transfer coordinate by *a* factor of four at 400 K and by *a* factor of around two at 600 K. Hence, NQEs do cause quantitative differences in proton transfer in the hexatic phase. We again compute the joint free energy distribution of the proton transfer coordinate ν and the oxygen–oxygen distance d_{OO}, as shown in Fig. 3(c). The changes to the d_{OO} distance distribution

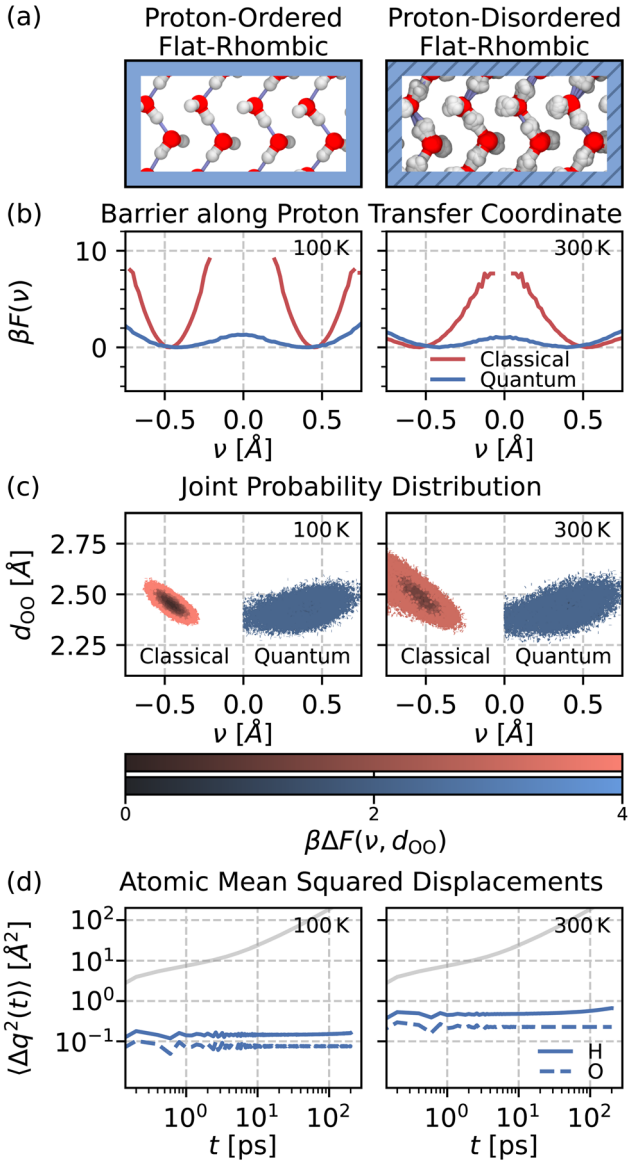

Fig. 2 Proton disorder in nanoconfined ice. (a) Snapshots of the flat-rhombic phase without (left) and with (right) nuclear quantum effects, illustrating proton order and disorder, respectively. The right snapshot shows all 32 beads from our path-integral molecular dynamics simulations. (b) Free energy profiles along the proton transfer coordinate ν for the flat-rhombic phase without (red) and with (blue) nuclear quantum effects at 100 K (left) and 300 K (right). (c) Joint free energy profiles of neighboring oxygen–oxygen distances d_{OO} and ν for the flat-rhombic phases at 100 K (left) and 300 K (right). Darker regions correspond to lower free energies. The distributions are symmetric about ν by definition, so only classical (red) distributions are shown for negative ν and quantum (blue) for positive ν. (d) Mean squared displacement of protons (solid lines) and oxygen atoms (dashed lines). The grey curve shows the characteristic diffusive mean-squared displacement for the superionic phase, taken from path-integral molecular dynamics simulations of the superionic hexatic phase at 600 K.

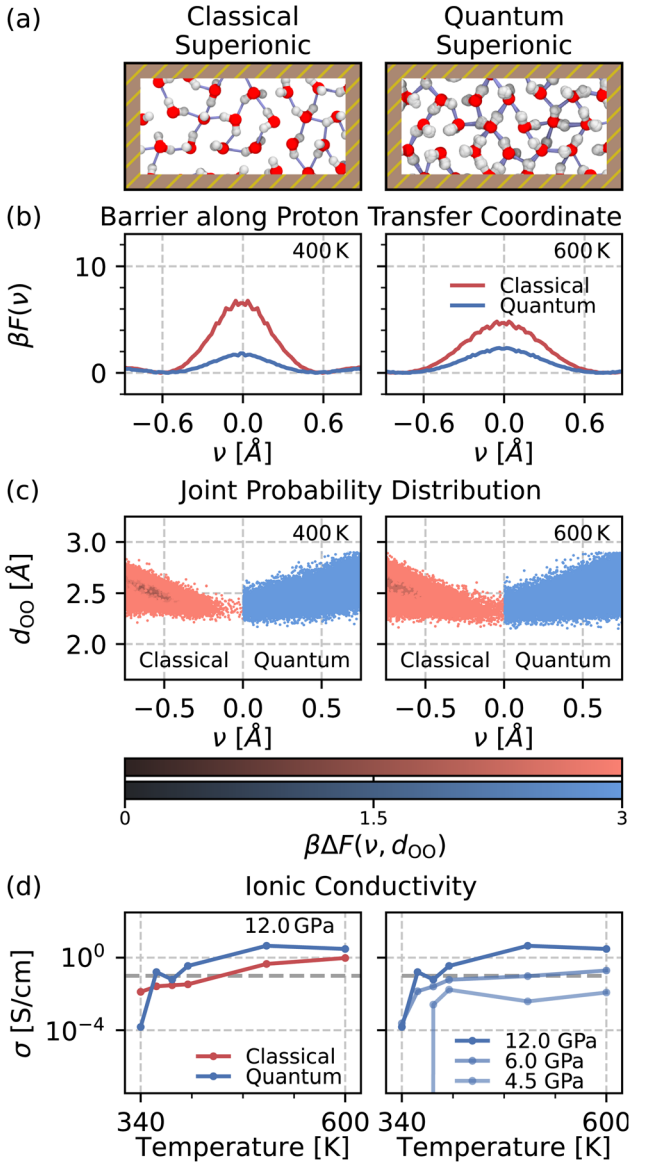

Fig. 3 Enhanced ionic conductivity in hexatic water. (a) Snapshots of the superionic hexatic phase without (left) and with (right) nuclear quantum effects. The right snapshot shows all 32 beads from our path-integral molecular dynamics simulations. No substantial qualitative difference is visible. (b) Free energy profiles along the proton transfer coordinate ν for the hexatic phase without (red) and with (blue) nuclear quantum effects at 100 K (left) and 300 K (right). (c) Joint free energy profile of neighbouring oxygen–oxygen distances d_{OO} and ν for the hexatic phase at 100 K (left) and 300 K (right). Darker regions correspond to lower free energies. The distributions are symmetric about ν by definition, so only classical (red) distributions are shown for negative ν and quantum (blue) for positive ν. (d) The left panel shows the classical and quantum ionic conductivities of the hexatic phase at 12 GPa. The right panel shows the quantum ionic conductivity at 4.5, 6.0 and 12.0 GPa. For both panels, the 0.1 S cm^{-1} superionic threshold is shown with a dashed grey line.

between the classical and quantum simulations are much more modest in the hexatic phase than the changes observed in the flat-rhombic phase. However, the inclusion of NQEs still leads to greater excursions along the proton-transfer coordinate for a given d_{OO} value, as we saw previously.

Unlike in the flat-rhombic phase, this proton delocalisation is associated with long-range proton transfer in the hexatic

phase (see Section V of the SI). In bulk water, long-range proton diffusion relies on the collective motion of neighbouring water molecules to enable proton hopping.[52] The ordered structure of the flat-rhombic phase inhibits collective reorganisation of water molecules, which may explain the absence of long-range proton diffusion. In contrast, the rotational disorder in the hexatic phase facilitates rearrangements of neighbouring water molecules, supporting proton transfer between adjacent sites. This long-range proton transfer suggests an increase in the overall ionic conductivity. To confirm this, we calculate the classical and quantum ionic conductivity in Fig. 3(d) using the Einstein–Helfand relations with classical and quantum simulations, respectively. With the inclusion of NQEs, the ionic conductivity of the disordered phase increases by over *a* factor of 10, which is likely due to zero-point O–H bond fluctuations. This surge in proton dissociation reduces the onset temperature for superionic behaviour from approximately 400 K to 360 K.

This NQE-induced enhancement of the ionic conductivity also occurs at lower lateral pressures. This is evidenced by the plots on the right side of Fig. 3(d), which show the ionic conductivity of monolayer water across the entire hexatic and liquid regime in the 4.5–12 GPa range. Estimating the classical and quantum ionic conductivity at low temperatures and pressures is statistically challenging due to the high variance associated with the microscopic ionic flux.[54] This can result in erroneously large values of ionic conductivities when the O–H bonds are bound at low temperatures and pressures. However, considering that superionic conductivity is driven by O–H dissociation, we estimate the ionic conductivity only for state points where we observe O–H dissociation events. The full details of our analysis are reported in Section V of the SI.

Conclusions

We have used machine learning-based first-principles simulations to investigate the influence of NQEs on proton delocalisation in monolayer nanoconfined water. The role of NQEs in these scenarios is stark. In the solid flat-rhombic phase, NQEs cause proton shuttling between neighbouring oxygen atoms. As we do not observe such shuttling anywhere in our classical simulations, these motions appear to be strongly suppressed for classical nuclei under the conditions studied. Their enhancement with the inclusion of NQEs may arise from proton tunnelling and/or other quantum effects, such as zero-point motion. In the hexatic phase, NQEs significantly enhance water's ionic conductivity. The superionic region within the phase diagram is greatly expanded, with nearly the entire hexatic region above 6 GPa exhibiting superionicity. Even at 3 GPa, where we do not observe superionic behaviour, water becomes partially dissociated within the nanosecond timescale. Considering that water encapsulated between graphene sheets experiences lateral pressures around 1–2 GPa, our simulations suggest that current experimental setups could observe high (if not superionic) conductivities. Indeed, recent work by Wang *et al.*[55] reports high ionic conductivity of water in nanocapillaries with widths below 1 nanometer. Overall, our work emphasises the need to include NQEs in simulations of nanofluidic transport, even under conditions where NQEs are minor in bulk systems.

Author contributions

P. R., A. M., and V. K. conceived and designed the research. P. R. performed the simulations. All authors contributed to data analysis and interpretation. P. R. and V. K. wrote the first draft of the manuscript, and all authors reviewed and edited the final version.

Conflicts of interest

There are none to declare.

Data availability

Input files and scripts are available: https://github.com/venkatkapil24/data-superionic-monolayer-with-nqes.

Supplementary information (SI): computational details, validation of revPBE0-D3 and the MLIP for O–H dissociation, a definition of the proton transfer coordinate ν, and additional analyses of proton transfer and ionic conductivity across pressures and temperatures in the flat-rhombic and hexatic phases. See DOI: https://doi.org/10.1039/d6sc00138f.

Acknowledgements

P. R. thanks David R. Reichman for his academic support and the Winston Churchill Foundation of the United States for their financial support. X. R. A, S. W. C, and A. M. acknowledge support from the European Union under the "n-AQUA" European Research Council project (Grant no. 101071937). B. X. S. acknowledges support from the EPSRC Doctoral Training Partnership (EP/T517847/1). V. K. acknowledges the Ernest Oppenheimer Early Career Fellowship and the Sydney Harvey Junior Research Fellowship, Churchill College, University of Cambridge, as well as startup funds from UCL. We are grateful for computational support from the Swiss National Supercomputing Centre under project s1209, the UK national high-performance computing service, ARCHER2, for which access was obtained *via* the UKCP consortium and the EPSRC grant ref EP/P022561/1, the Cambridge Service for Data Driven Discovery (CSD3) and the Cirrus UK National Tier-2 HPC Service at EPCC (http://www.cirrus.ac.uk) funded by the University of Edinburgh and EPSRC (EP/P020267/1) P.R. acknowledges that: "This material is based upon work supported by the U.S. Department of Energy, Office of Science, Office of Advanced Scientific Computing Research, Department of Energy Computational Science Graduate Fellowship under Award Number DE-SC0024386." P. R. also makes the disclaimer that: "This report was prepared as an account of work sponsored by an agency of the United States Government. Neither the United States Government nor any agency thereof, nor any of their employees, makes any warranty, express or implied, or assumes any legal liability or responsibility for the accuracy, completeness, or usefulness of any information, apparatus, product, or process

disclosed, or represents that its use would not infringe privately owned rights. Reference herein to any specific commercial product, process, or service by trade name, trademark, manufacturer, or otherwise does not necessarily constitute or imply its endorsement, recommendation, or favoring by the United States Government or any agency thereof. The views and opinions of authors expressed herein do not necessarily state or reflect those of the United States Government or any agency thereof."

References

1 C. G. Salzmann, *J. Chem. Phys.*, 2019, **150**, 060901.
2 E. Burton and W. Oliver, *Proc. R. Soc. London, A*, 1935, **153**, 166–172.
3 T. Loerting, C. Salzmann, I. Kohl, E. Mayer and A. Hallbrucker, *Phys. Chem. Chem. Phys.*, 2001, **3**, 5355–5357.
4 R. J. Nelmes, J. S. Loveday, T. Strässle, C. L. Bull, M. Guthrie, G. Hamel and S. Klotz, *Nat. Phys.*, 2006, **2**, 414–418.
5 A. Rosu-Finsen, M. B. Davies, A. Amon, H. Wu, A. Sella, A. Michaelides and C. G. Salzmann, *Science*, 2023, **379**, 474–478.
6 K. H. Kim, K. Amann-Winkel, N. Giovambattista, A. Späh, F. Perakis, H. Pathak, M. L. Parada, C. Yang, D. Mariedahl, T. Eklund, *et al.*, *Science*, 2020, **370**, 978–982.
7 G. Algara-Siller, O. Lehtinen, F. Wang, R. R. Nair, U. Kaiser, H. Wu, A. K. Geim and I. V. Grigorieva, *Nature*, 2015, **519**, 443–445.
8 V. Kapil, C. Schran, A. Zen, J. Chen, C. J. Pickard and A. Michaelides, *Nature*, 2022, **609**, 512–516.
9 B. Lin, J. Jiang, X. C. Zeng and L. Li, *Nat. Commun.*, 2023, **14**, 4110.
10 J. Jiang, Y. Gao, L. Li, Y. Liu, W. Zhu, C. Zhu, J. S. Francisco and X. C. Zeng, *Nat. Phys.*, 2024, **20**, 456–464.
11 S. Li and B. Schmidt, *Phys. Chem. Chem. Phys.*, 2019, **21**, 17640–17654.
12 N. Giovambattista, P. Rossky and P. Debenedetti, *Annu. Rev. Phys. Chem.*, 2012, **63**, 179–200.
13 E. Secchi, S. Marbach, A. Niguès, D. Stein, A. Siria and L. Bocquet, *Nature*, 2016, **537**, 210–213.
14 K. Gopinadhan, S. Hu, A. Esfandiar, M. Lozada-Hidalgo, F. Wang, Q. Yang, A. Tyurnina, A. Keerthi, B. Radha and A. Geim, *Science*, 2019, **363**, 145–148.
15 L. Fumagalli, A. Esfandiar, R. Fabregas, S. Hu, P. Ares, A. Janardanan, Q. Yang, B. Radha, T. Taniguchi, K. Watanabe, *et al.*, *Science*, 2018, **360**, 1339–1342.
16 N. Kavokine, M.-L. Bocquet and L. Bocquet, *Nature*, 2022, **602**, 84–90.
17 S. Han, M. Choi, P. Kumar and H. E. Stanley, *Nat. Phys.*, 2010, **6**, 685–689.
18 J. C. Johnston, N. Kastelowitz and V. Molinero, *J. Chem. Phys.*, 2010, **133**, 154516.
19 H. Kumar, B. Mukherjee, S.-T. Lin, C. Dasgupta, A. Sood and P. K. Maiti, *J. Chem. Phys.*, 2011, **134**, year.
20 J. Zubeltzu, F. Corsetti, M. Fernández-Serra and E. Artacho, *Phys. Rev. E*, 2016, **93**, 062137.
21 F. Corsetti, P. Matthews and E. Artacho, *Sci. Rep.*, 2016, **6**, 18651.
22 J. Chen, A. Zen, J. G. Brandenburg, D. Alfè and A. Michaelides, *Phys. Rev. B*, 2016, **94**, 220102.
23 J. Chen, G. Schusteritsch, C. J. Pickard, C. G. Salzmann and A. Michaelides, *Phys. Rev. Lett.*, 2016, **116**, 025501.
24 P. Ravindra, X. R. Advincula, C. Schran, A. Michaelides and V. Kapil, *Nat. Commun.*, 2024, **15**, 7301.
25 J. Jiang, Y. Gao, W. Zhu, Y. Liu, C. Zhu, J. S. Francisco and X. C. Zeng, *J. Am. Chem. Soc.*, 2021, **143**, 8177–8183.
26 R. Husband, H. Liermann, J. McHardy, R. McWilliams, A. Goncharov, V. Prakapenka, E. Edmund, S. Chariton, Z. Konôpková, C. Strohm, *et al.*, *Nat. Commun.*, 2024, **15**, 8256.
27 M. Millot, S. Hamel, J. R. Rygg, P. M. Celliers, G. W. Collins, F. Coppari, D. E. Fratanduono, R. Jeanloz, D. C. Swift and J. H. Eggert, *Nat. Phys.*, 2018, **14**, 297–302.
28 M. Millot, F. Coppari, J. R. Rygg, A. Correa Barrios, S. Hamel, D. C. Swift and J. H. Eggert, *Nature*, 2019, **569**, 251–255.
29 J. Sun, B. K. Clark, S. Torquato and R. Car, *Nat. Commun.*, 2015, **6**, 8156.
30 M. Flór, D. M. Wilkins, M. de la Puente, D. Laage, G. Cassone, A. Hassanali and S. Roke, *Science*, 2024, **386**, eads4369.
31 K.-Y. Chiang, J. Hunger, M. Bonn and Y. Nagata, *Sci. Adv.*, 2025, **11**, eadv7218.
32 S. Habershon, T. E. Markland and D. E. Manolopoulos, *J. Chem. Phys.*, 2009, **131**, 024501.
33 X.-Z. Li, B. Walker and A. Michaelides, *Proc. Natl. Acad. Sci. U. S. A.*, 2011, **108**, 6369–6373.
34 M. Ceriotti, W. Fang, P. G. Kusalik, R. H. McKenzie, A. Michaelides, M. A. Morales and T. E. Markland, *Chem. Rev.*, 2016, **116**, 7529–7550.
35 M. Benoit, D. Marx and M. Parrinello, *Nature*, 1998, **392**, 258–261.
36 S. Jiao, C. Duan and Z. Xu, *Sci. Rep.*, 2017, **7**, 2646.
37 J. Behler, *Int. J. Quantum Chem.*, 2015, **115**, 1032–1050.
38 P. R. Nagy and M. Kállay, *J. Chem. Theory Comput.*, 2019, **15**, 5275–5298.
39 V. Kapil, M. Rossi, O. Marsalek, R. Petraglia, Y. Litman, T. Spura, B. Cheng, A. Cuzzocrea, R. H. Meißner, D. M. Wilkins, *et al.*, *Comput. Phys. Commun.*, 2019, **236**, 214–223.
40 A. Singraber, J. Behler and C. Dellago, *J. Chem. Theor. Comput.*, 2019, **15**, 1827–1840.
41 A. P. Thompson, H. M. Aktulga, R. Berger, D. S. Bolintineanu, W. M. Brown, P. S. Crozier, P. J. In't Veld, A. Kohlmeyer, S. G. Moore, T. D. Nguyen, *et al.*, *Comput. Phys. Commun.*, 2022, **271**, 108171.
42 F. Musil, I. Zaporozhets, F. Noé, C. Clementi and V. Kapil, *J. Chem. Phys.*, 2022, **157**, 181102.
43 J. Cao and G. A. Voth, *J. Chem. Phys.*, 1993, **99**, 10070–10073.
44 J. M. Kosterlitz and D. Thouless, *J. Phys. C: Solid State Phys.*, 1972, **5**, L124.
45 J. M. Kosterlitz and D. J. Thouless, in *Basic Notions Of Condensed Matter Physics*, CRC Press, 2018, pp. 493–515.

46 T. E. Markland and D. E. Manolopoulos, *Chem. Phys. Lett.*, 2008, **464**, 256–261.
47 A. Reinhardt and B. Cheng, *Nat. Commun.*, 2021, **12**, 588.
48 B. Cheng, M. Bethkenhagen, C. J. Pickard and S. Hamel, *Nat. Phys.*, 2021, **17**, 1228–1232.
49 M. Ceriotti, J. Cuny, M. Parrinello and D. E. Manolopoulos, *Proc. Natl. Acad. Sci. U. S. A.*, 2013, **110**, 15591–15596.
50 A. Hassanali, F. Giberti, J. Cuny, T. D. Kühne and M. Parrinello, *Proc. Natl. Acad. Sci. U. S. A.*, 2013, **110**, 13723–13728.
51 C. Richter, D. Hollas, C.-M. Saak, M. Förstel, T. Miteva, M. Mucke, O. Björneholm, N. Sisourat, P. Slavíček and U. Hergenhahn, *Nat. Commun.*, 2018, **9**, 4988.
52 N. Agmon, *Chem. Phys. Lett.*, 1995, **244**, 456–462.
53 K.-D. Kreuer, *Chem. Mater.*, 1996, **8**, 610–641.
54 F. Grasselli and S. Baroni, *Nat. Phys.*, 2019, **15**, 967–972.
55 R. Wang, M. Souilamas, A. Esfandiar, R. Fabregas, S. Benaglia, H. Nevison-Andrews, Q. Yang, J. Normansell, P. Ares, G. Ferrari *et al.*, *In-Plane Dielectric Constant And Conductivity Of Confined Water*, 2024.